Title

Establishing the Role of Operating Potential and Mass Transfer in Multicarbon Product Generation for Photoelectrochemical CO2 Reduction Cells Using a Cu Catalyst

Journal

ACS Energy Letters, 7(8)

ISSN

2380-8195

Authors

King, Alex J
Bui, Justin C
Bell, Alexis T
et al.

Publication Date

2022-08-12

DOI

10.1021/acsenergylett.2c01041

Peer reviewed

Establishing the Role of Operating Potential and Mass Transfer in Multicarbon Product Generation for Photoelectrochemical CO_2 Reduction Cells Using a Cu Catalyst

Alex J. King[1,2], Justin C. Bui [1,2], Alexis T. Bell*[1,2], and Adam Z. Weber*[2]

[1] Department of Chemical and Biomolecular Engineering
University of California Berkeley
Berkeley, CA 94720, USA

[2] Liquid Sunlight Alliance
Lawrence Berkeley National Laboratory
Berkeley, CA 94720, USA

*To whom correspondence should be sent: alexbell@berkeley.edu; azweber@lbl.gov

Abstract

There is increasing interest in the possibility of photoelectrochemical (PEC) reduction of CO_2 to C_{2+} products; however, the criteria for maximizing PEC solar-to-C_{2+} (STC_{2+}) rates are not well understood. We report here a continuum-scale model of PEC CO_2 reduction (CO_2R) on Cu in 0.1 M $CsHCO_3$ and use it to optimize the design and operating conditions for generating C_{2+} products. We demonstrate that the potential-dependent product distribution of CO_2R on Cu requires operating near the potential that maximizes C_{2+} generation rates (V_{id}), unlike PEC water splitting that desires operation at the maximum photocurrent density. Because of this requirement, the criterion for a high STC_{2+} rate includes high photocurrent semiconductors with photovoltages near V_{id} and low series resistance. The STC_{2+} rate in these systems is enhanced by optimal CO_2 transport and exhibits low sensitivity to solar irradiance variations from the diurnal cycle.

Photoelectrochemical (PEC) cells have attracted considerable attention for their potential to convert solar energy directly into chemical bonds, easing storage and transport concerns.[1–6] While significant research focused on PEC water splitting to generate hydrogen,[1,2,5–12,13,14] PEC carbon-dioxide reduction (CO_2R) has only recently begun to receive substantial interest for generating fuels and chemicals from CO_2 directly.[15–21]

Prior PEC CO_2R work has focused primarily on photocathodes producing single-carbon (C_1) products;[15,16,20,22,23] however, the production of multicarbon (C_{2+}) products is more attractive because of their higher energy density, large market demand, and compatibility with established infrastructure.[21,24] Copper (Cu) has the unique ability to catalyze CO_2R to C_{2+} products with high faradaic efficiency (FE),[24,25] leading to its examination for PEC CO_2R.[21,23,26] While various Cu-based oxides and chalcogenides have been investigated as photocathodes, these materials produce primarily H_2 and C_1 products.[23] Alternatively, photocathodes containing metallic Cu deposited on a semiconductor were reported to generate C_{2+} products at appreciable rates and selectivities.[21,23,26]

The product distribution of electrochemical CO_2R on Cu is highly potential dependent,[25] as is that of PEC CO_2R on the photocathode potential.[21,27] This inherent potential-dependent selectivity presents challenges for the design and operation of PEC CO_2R systems that are distinct from those for PEC systems designed for water splitting. For water splitting, the single product H_2 generation rate is optimized by operation at the maximum photocurrent.[1,2,28] By contrast, the CO_2R product distribution requires operation at the potential that maximizes the desired product rate (a combination of selectivity and total rate), which may not occur at the maximum photocurrent. Reactant transport is a more critical consideration for efficient PEC CO_2R than PEC water splitting as CO_2 is sparingly soluble in aqueous electrolytes and it must transverse a boundary layer to reach the electrode surface, whose thickness depends on the electrolyte flowrate (or the non-dimensional

Reynolds number).[29] Because of these factors, CO_2 transport can limit CO_2R current densities to ~20 mA cm^{-2} in bicarbonate electrolytes.[30]

Previous PEC CO_2R modeling efforts have explored device architectures,[31,32] reaction mechanisms,[33–36] and multi-scale modeling approaches.[33,35] In this report, we build upon the prior computational work by presenting a model for simulating the performance of PEC CO_2R, which accounts for photo-absorber performance, catalyst kinetics, and mass transport through the boundary layer. This model is then used to define the operating conditions and design considerations required for optimal solar-to-C_{2+} (STC_{2+}) rates, as well as reveal how the PEC device performs with changing electrolyte environment directly adjacent to the catalyst surface (microenvironment). Next, we examine impacts of solar irradiance on product selectivity and how to mitigate it. A summary of the findings is provided in **Table S4**. A schematic of the modeled system is shown in **Figure 1A** (see SI **Section S1** for details). CO_2 diffuses through a mass-transport boundary layer and reacts on the surface of Cu to form H_2, C_1 (HCOOH, CO, and CH_4), and C_{2+} (C_2H_4, EtOH, PrOH, and AllylOH) products via the concentration-dependent Tafel equation (kinetic parameters are provided in **Table S3**). The driving force for this process is the semiconductor-generated photovoltage. The species concentrations at the bulk-electrolyte boundary are those present in 0.1 M $CsHCO_3$ saturated with CO_2.[37,38] $CsHCO_3$ is chosen because of its buffering capacity and high C_{2+} production rate due to Cs^+ electric-field stabilizing effect on adsorbed intermediates.[38–41] The solar cell is simulated by the ideal-diode equation in the Shockley-Queisser radiative efficiency limit, assuming AM 1.5G solar illumination. The governing equations are solved using COMSOL Multiphysics 5.5 software, and the photovoltaic (PV) equations and the intersection point between the solar power curve of the PV and the load

curve for the electrolyzer is determined using the Python NumPy library (see SI **Section S2** for details and **Tables S1-S3** for physical parameters).

While the model presented here can predict general PV performance requirements for high STC_{2+}, it is inadequate for predicting specific semiconductor properties to achieve a set performance level because of the simplicity of the semiconductor physics. Other factors, such as dry- vs wet-side illumination, semiconductor doping concentration, band bending, interfacial barrier heights, and surface defects, are neglected but will ultimately influence PV performance.[1,5,9–11,42] We also do not address the form of the Cu catalyst, *i.e.*, whether it is a thin film or nanoparticles, recognizing that these factors also impact PEC performance by altering the electrochemically active surface area, kinetics, fraction of reflected light, and the Schottky barrier height.[1,42,43] Incorporating such factors is outside the scope of this current study, which is to provide general performance guidelines for achieving high STC_{2+} rates. Moreover, their impact on PEC performance is implicitly seen when altering illumination intensity, series resistance, and shunt resistance because they principally modify the photocurrent, photovoltage, and fill factor (**Figure S1**). Therefore, incorporation of the above factors is not expected to change the conclusions of this study.

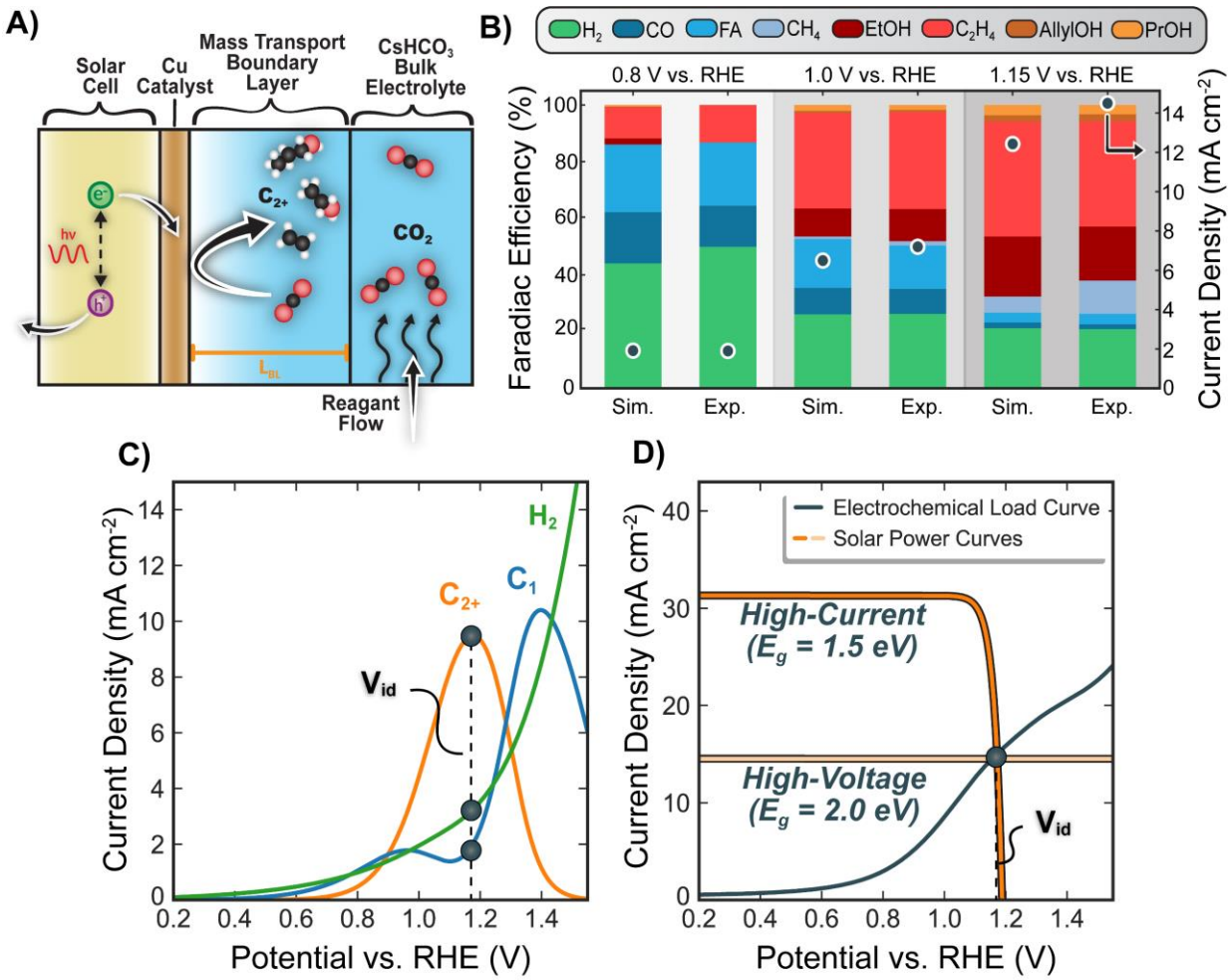

Figure 1: (A) Illustration of modeled system. **(B)** Comparison of simulated and experimentally measured product FEs (stacked bars) and total current densities (markers). **(C)** Partial current densities of H_2 (green), C_1 (blue), and C_{2+} (orange) as a function of cathode potential. **(D)** Intersection of electrochemical load curve and solar power curves for high-current (1.5 eV bandgap) and high-voltage (2.0 eV bandgap) PVs that each intersect the load curve at V_{id}, the voltage that maximizes C_{2+} formation rate.

Figure 1B compares the effect of cathode potential on the product distribution obtained from the electrochemical model to the data of Kim *et al.*[44] for a roughened, planar Cu cathode performing dark electrolysis in 0.1 M $CsHCO_3$. The good agreement validates the electrochemical model and fitted kinetic parameters, which are taken to remain the same irrespective of illumination.[21] **Figure 1C** displays the simulated partial current densities of H_2, C_1, and C_{2+} products as a function of potential, showing that the rate of C_{2+} generation peaks at V_{id}. The

decreased C_{2+} current density at high potentials is a result of the low surface CO_2 concentration and a shift to CH_4 because of its high transfer coefficient (**Table S3**).[29] For PEC systems, the operating point is the intersection between the total electrochemical load and solar power curves,[8,14,32] as shown in **Figure 1D** for semiconductors with bandgaps of 1.5 and 2.0 eV. Both semiconductors lead to PEC operation at V_{id}, which maximizes the STC_{2+} rate. Semiconductors with bandgaps other than 1.5 and 2.0 eV lead to solar power curves that do not intersect the electrochemical load curve at V_{id}, and, as a result, will not lead to the maximum STC_{2+} rate, although they could lead to higher total current densities (*e.g.*, as would be desired for water splitting) (see SI **Section S5** and **Figures S2-S4**); only semiconductors with bandgaps of 1.5 eV and 2.0 eV are considered for the remainder of the analysis, and are referred to as high-current and high-voltage photocathodes, respectively. While InP, GaAs, and CdTe and GaInP, GaAsP, and InAlAs semiconductors have ~1.5 eV and ~2.0 eV bandgaps, respectively,[45,46] these materials may not lead to the maximal STC_{2+} rate because of differences in V_{id} between systems and/or poor carrier transport across the metal-semiconductor interface. To promote high STC_{2+} rates, identifying V_{id} and i_{id} for the Cu catalyst of interest and integrating it with semiconductor(s) that can operate near those conditions is paramount.

Solar-to-hydrogen efficiency is a key variable being optimized in PEC water splitting, and is maximized at the max power point (P_{max}) on the solar power curve.[1,2,28] For PEC CO_2R, however, P_{max} is likely not to occur at V_{id}, which gives rise to a maximum STC_{2+} efficiency not located at P_{max}. **Figure S3** shows that operating at P_{max} leads to a STC_{2+} rate of ~0.5 mA cm^{-2} but operating at V_{id} generates a STC_{2+} rate of ~9.5 mA cm^{-2}, a 19x greater STC_{2+} efficiency. This further emphasizes the distinct requirements for high performing PEC water splitting and CO_2R systems. While STC_{2+} efficiency is a key figure of merit, we choose to focus on STC_{2+} rates instead

to separate changes in C_{2+} current density from changes in other factors that influence efficiency (*i.e.*, solar insolation). In general, the trends in STC_{2+} rates presented here will correlate to STC_{2+} efficiency, since they are directly related (see **Section S1** for definitions).[17,28]

The effect of mass transport on PEC CO_2R operation is presented in **Figure 2A** for the high-current and high-voltage photocathodes as a function of Reynolds number (Re). Changing Re varies the CO_2 diffusion length and changes the electrochemical performance. For the high-current photocathode, intersection of the load curve occurs on the steep, nearly vertical segment of the solar power curve, and, consequently, the operating current density of this PEC device increases with Re, whereas the operating potential changes very little. However, the high-voltage photocathode is photocurrent limited and, therefore, the operating current density is constant with Re, resulting in considerable operating potential changes.

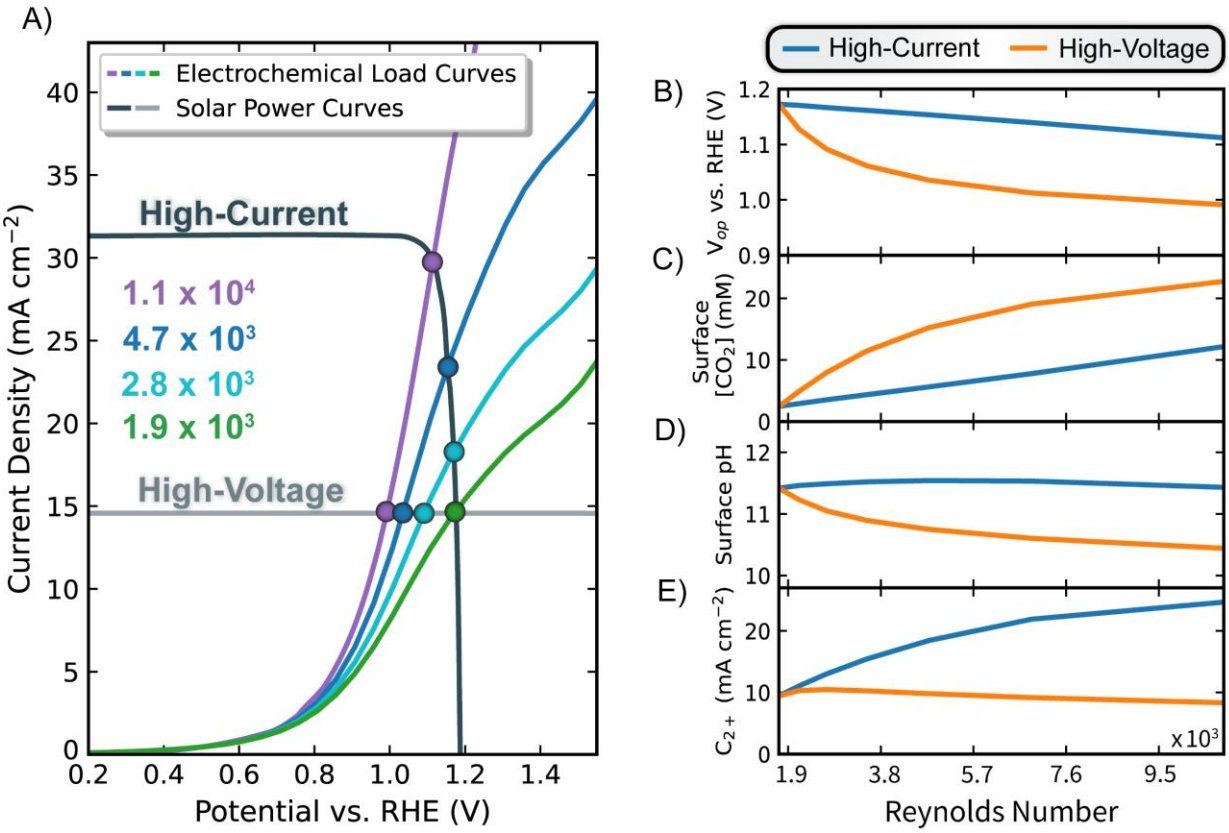

Figure 2: (A) PEC operating point for the high-current (1.5 eV bandgap) and high-voltage (2.0 eV bandgap) systems at various Reynolds numbers. **(B)** Operating potential (V_{op}), **(C)** electrode surface CO_2 concentration, **(D)** electrode surface pH, and **(E)** C_{2+} current density (C_{2+}) as a function of Reynolds number for the high-current (blue line) and high-voltage (orange line) PEC systems.

As seen in in **Figure 2B**, significant operating potential changes (~ 200 mV) occur for the high-voltage photocathode, but < 80 mV for the high-current photocathode. It is important to note that V_{id} increases logarithmically with Re; although, beyond 10 mL min^{-1}, the shift is small (< 70 mV) and, thus, V_{id} is approximately constant (**Figure S6**). In addition to altering the operating potential, varying the Re also modifies the local CO_2 concentration and pH adjacent to the Cu surface; high values of both variables are known to enhance C_{2+} product selectivity.[29,39,44,47] **Figure 2C** demonstrates that the CO_2 concentration at the Cu surface increases with Re regardless of the semiconductor properties due to the thinner mass-transport boundary layer (decreasing from 100 to 40 μm as the Re increases from 1.9×10^3 to 1.1×10^4). For the high-voltage photocathode, the surface CO_2 concentration increases non-linearly with Re, as opposed to the linear trend for the high-current photocathode, because the change in operating potential shifts the product distribution to more C_1 products, which consumes less CO_2 than C_{2+} products. The surface pH, however, is relatively constant for the high-current photocathode but decreases ~1 pH-unit for the high-voltage photocathode when the Re increases an order of magnitude, see **Figure 2D**. This decrease in the surface pH is attributed to the thin boundary layer at high Re, reducing the distance between the surface and bulk electrolyte. Species concentration profiles within the boundary layer are provided in **Figure S10**. Despite the improved surface CO_2 concentration, the low operating potential for the high-voltage photocathode system hinders STC_{2+} rates at large Re, **Figure 2E**.

The STC_{2+} rate for the high-voltage photocathode increases marginally just above 1.9×10^3 Re but reduces with Re beyond 2.5×10^3. However, the relatively stable operating

potential of the high-current photocathode enables this system to access a state of enhanced local CO_2 concentration and high surface pH while operating near V_{id}, thereby significantly improving the rate of STC_{2+}, underscoring the importance of potential on product selectivity. The decreasing slope in the STC_{2+} rate for the high-current photocathode seen in **Figure 2E** results from minor reductions in operating potential, indicating a threshold Re beyond which the rate of STC_{2+} does not increase. These results are highlighted further in **Figure S5**, which shows a ~1.5 eV bandgap (high-current photocathode) is the only system that experiences significant enhancements in STC_{2+} rates with Re because its operating potential remains near V_{id}. The results shown here emphasize the importance of effective cathode potential when seeking optimal mass transfer for improved rates of STC_{2+} in PEC CO_2R systems.

An analysis similar to that given above is conducted for bulk $CsHCO_3$ concentration and is shown in **Figures S7** and **S8**. Upon increasing the $CsHCO_3$ concentration from 0.1 to 0.4 M, the high-current photocathode experiences a ~2.5 mA cm^{-2} increase in STC_{2+} rate due to greater electrode surface CO_2 concentration; further increases in electrolyte concentration decreases the rate of STC_{2+} because of the decrease in operating potential. For the high-voltage photocathode, the significant decrease in operating potential causes the STC_{2+} rate to decrease with increasing $CsHCO_3$ concentration. A detailed discussion on the effect of bulk electrolyte concentration on STC_{2+} rates is provided in **Section S8**.

Because of the dependence of product distribution on operating potential, changes in solar illumination intensity can also alter the STC_{2+} rate. **Figure 3A** and **B** shows the operating point for the high-current photocathode is relatively stable at > 50 mW cm^{-2} intensity whereas the high-voltage photocathode operating point changes substantially for all intensities up to one sun, neglecting any changes in light wavelength. As a result, the high-current photocathode reaches V_{id}

and the largest STC_{2+} rate at much lower intensities than the high-voltage photocathode, and remains fairly stable, see **Figure 3C** and **D**. This difference results from the larger photocurrent generated by the high-current photocathode, enabling device operation closer to V_{id} at lower intensities compared to the high-voltage photocathode. Further disparity between high-current and high-voltage photocathodes exists with variable series and shunt resistances as seen in **Figure S9**, which demonstrates that high-current and high-voltage photocathodes must have low series and low shunt resistances, respectively, to achieve high STC_{2+} rates (see **Section S9** for details). These findings indicate that PEC devices operated with a high-current photocathode and low series resistances are superior to high-voltage photocathodes under conditions of dynamic illumination intensity due to their lower sensitivity to changes in operating potential.

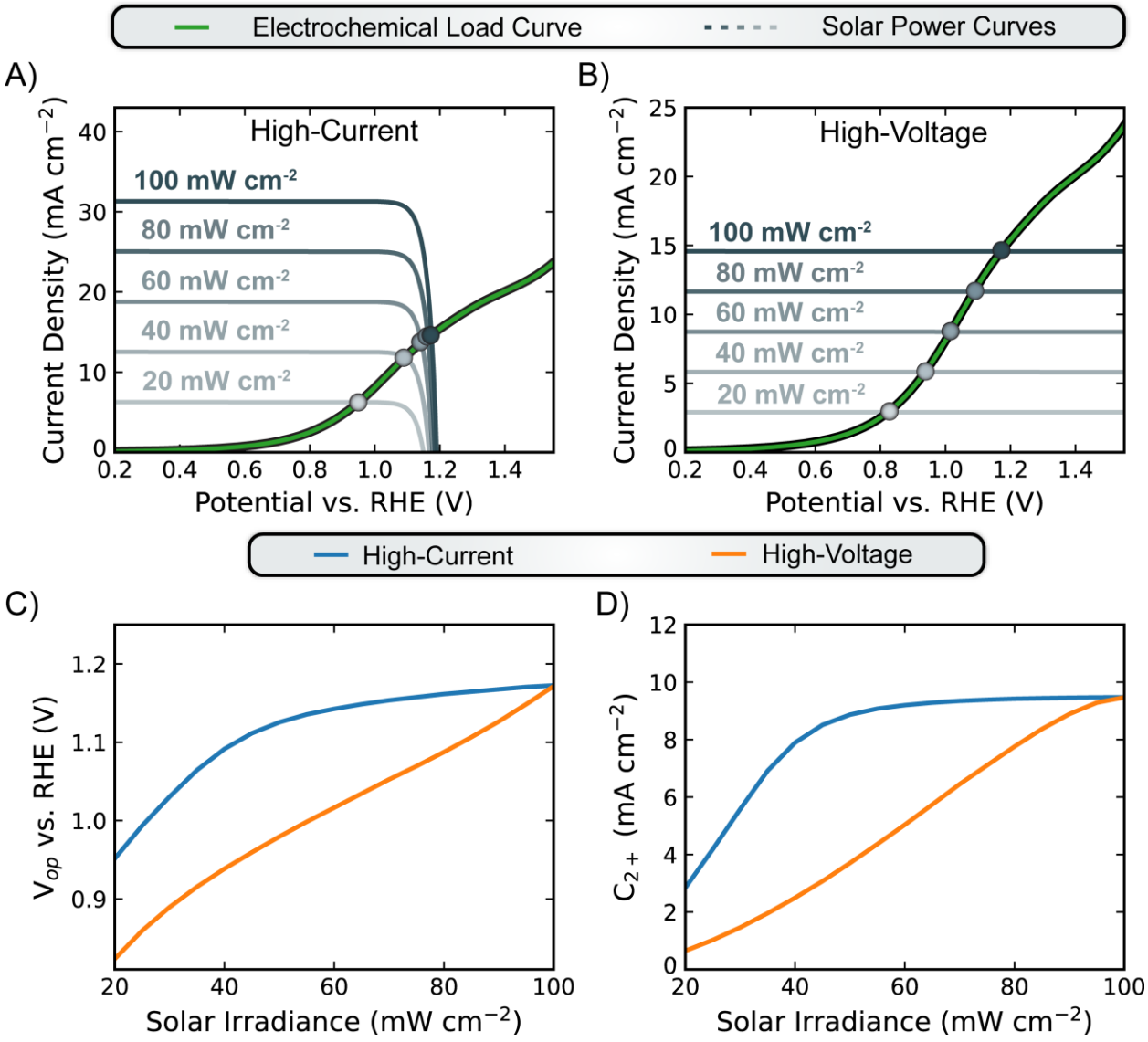

Figure 3: Operating points at various illumination intensities with a Re of 1.9×10^3 for the **(A)** high-current and **(B)** high-voltage photocathodes. **(C)** Operating potential and **(D)** solar-to-C_{2+} rate (C_{2+}) for the high-current and high-voltage photocathode.

The influence of Re and solar irradiance on the rate of STC_{2+} suggests that CO_2 transport management could minimize losses in STC_{2+} rates due to solar-irradiance variations. To explore this strategy, we identified the hourly optimal Re for the two PEC systems assumed to be in Barstow, CA (**Figure 4A** provides the calculated irradiance from NREL TMY3 datasets for 2020 summer and winter solstices)[48] which currently hosts a large-scale PV power generation facility.[49]

It should be noted that AM 1.5G results in 100 mW cm^{-2} and no spectral data shift with time is assumed as discussed in **Figure S11**. **Figure 4** demonstrates the influence of hourly Re tuning at the two extremes of the sun's annual cycle. For comparison, a constant 1.9×10^3 Re operation is also considered since both PEC systems operate at V_{id} under full-sun illumination at this Re (see **Figure 2A**). The hourly optimum Re (**Figure 4B**) for both systems change in a similar manner with hourly irradiance. This is because of the increase in photocurrent with increasing intensity, which enables higher CO_2R rates at V_{id} through improved surface CO_2 concentration (high Re), see **Figure S13**. However, the high-current system results in optimal Re that greatly exceed the constant 1.9×10^3, whereas the high-voltage device operates at $\lesssim 1.9 \times 10^3$ for both the summer and winter solstices. **Figure 4C** demonstrates that only the high-current photocathode benefits substantially from dynamic tuning of CO_2 transport.

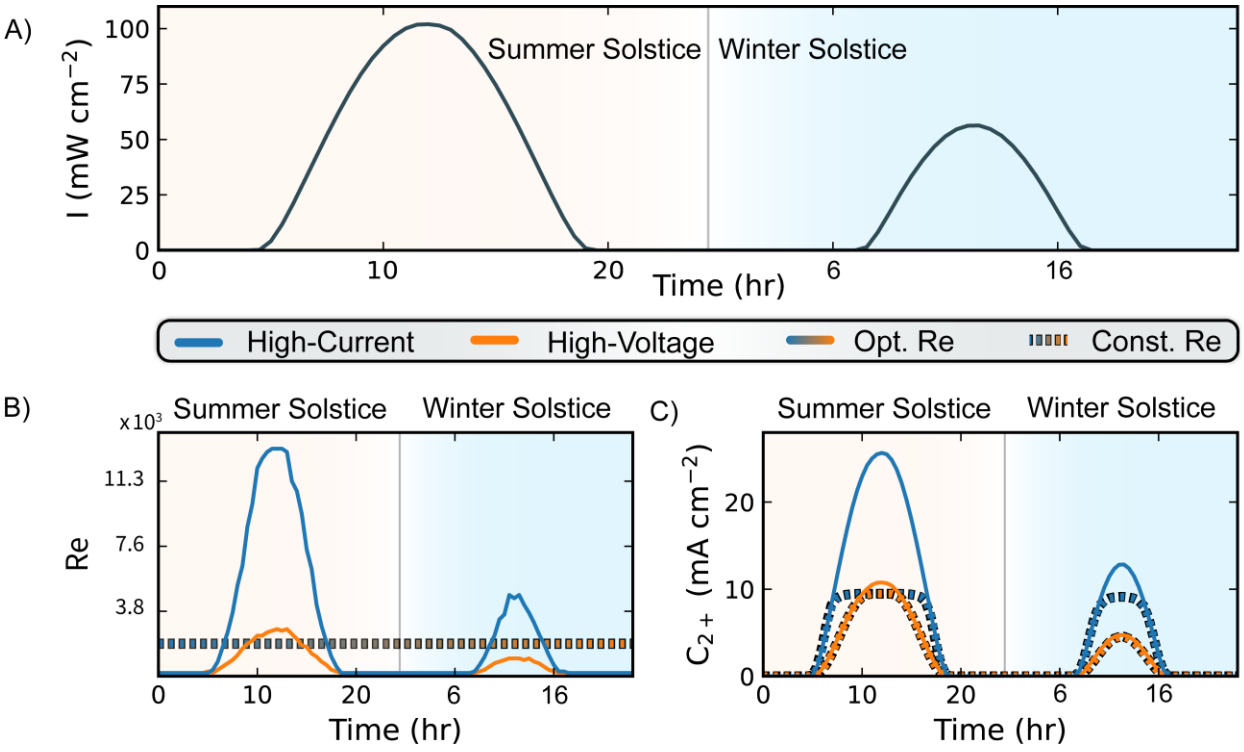

Figure 4: (A) Measured hourly solar irradiance (I) for Barstow, CA during the 2020 summer and winter solstices. Hourly **(B)** Reynolds number (Re) and **(C)** solar-to-C_{2+} rate (C_{2+}) for the summer and winter solstices.

For a constant electrolyte Re of 1.9×10^3, the rates of STC_{2+} for both systems reach the same maximum value at full sun during the summer solstice, as expected from **Figure 2**, but the high-current photocathode retains the maximum rate of STC_{2+} for longer durations (see **Figure 4C**). During the winter solstice, the rate of STC_{2+} for the high-current device is about double that of the high-voltage device at full sun, due to the lower sensitivity of the high-current system to variations in solar irradiance (**Figure 3**). The total amount of C_{2+} products generated in a day for the high-current device operating with an optimized Re is double that of the constant Re condition during the summer solstice and 1.2x greater during the winter solstice. The high-voltage system, on the other hand, experiences < 1.1x enhancement in C_{2+} products generated when operated with an optimized Re during the summer and winter solstices. This greater enhancement in STC_{2+} conversion with the high-current photocathode results from the significantly higher Re that are accessible while remaining near V_{id} (see **Figure S12**). Thus, for operation near V_{id}, tuning the CO_2 transport only enhances the STC_{2+} rate when the device is not photocurrent limited.

In summary, this study has used a multiphysics model to simulate the electrochemical and photovoltaic performances of PEC CO_2R systems using a Cu catalyst to promote the reduction of CO_2 to C_{2+} products. Management of the operating potential is key to achieving high solar-to-C_{2+} (STC_{2+}) rates. Furthermore, a PEC device with low series resistance that generates a high photocurrent at photovoltages near the potential for which the generation of C_{2+} products is maximized is ideally suited for high rates of STC_{2+}. This is because the slope of the solar power curve is steep and, consequently, limits variations in operating potential under dynamic conditions. As a result, such a device is capable of maximizing the rate of STC_{2+} throughout the day by

synchronizing the rate of CO_2 transport to the sun's diurnal and annual cycles. Such an optimum is different than the max power point as desired for solar water splitting, due to the dependence of product selectivity on local concentrations and potential. To improve predictions and design criteria, model improvements include incorporating band bending, metal-semiconductor interfacial barrier heights, surface defects, and semiconductor doping concentration. The findings of this study have critical implications for the practical design and operation of PEC CO_2R devices to achieve high rates of STC_{2+}.

Supporting Information

Outline and description of modeled physics; computational methods; summary of the impact of studied variables on C_{2+} generation rates; qualitative depiction of the influence of neglected factors on the solar power curve; C_{2+} formation rate change with bandgap and Reynolds number; variation of ideal operating potential; influence of varying bulk electrolyte concentration; PEC operation variations with varying photovoltaic performance; concentration profiles throughout boundary layer; AM 1.5G and Barstow spectral irradiance comparison; change in hourly operating point; operating point variations with Re and light intensity.

Acknowledgements

This material is based on work performed by the Liquid Sunlight Alliance, which is supported by the U.S. Department of Energy, Office of Science, Office of Basic Energy Sciences, Fuels from Sunlight Hub under Award Number DE-SC0021266. AJK acknowledges funding from the National Science Foundation Graduate Research Fellowship under Grant No. DGE 2146752. JCB acknowledges funding from the National Defense Science and Engineering Graduate Fellowship supported by the Army Research Office (ARO). We also acknowledge Chanyeon Kim for the experimental data of CO_2R on Cu, Francisco Galang for the operating-point identifier

algorithm, and Emily Warren, Joel Ager, and Sophia Haussener (affiliated with the Swiss Federal Institute of Technology Lausanne) for fruitful discussions on photovoltaic physics.

References

(1) Walter, M. G.; Warren, E. L.; McKone, J. R.; Boettcher, S. W.; Mi, Q.; Santori, E. A.; Lewis, N. S. Solar Water Splitting Cells. *Chem. Rev.* **2010**, *110* (11), 6446–6473. https://doi.org/10.1021/cr1002326.

(2) Hu, S.; Xiang, C.; Haussener, S.; Berger, A. D.; Lewis, N. S. An Analysis of the Optimal Band Gaps of Light Absorbers in Integrated Tandem Photoelectrochemical Water-Splitting Systems. *Energy Environ. Sci.* **2013**, *6* (10), 2984–2993. https://doi.org/10.1039/c3ee40453f.

(3) Quinn, J.; Hemmerling, J.; Linic, S. Maximizing Solar Water Splitting Performance by Nanoscopic Control of the Charge Carrier Fluxes across Semiconductor-Electrocatalyst Junctions. *ACS Catal.* **2018**, *8* (9), 8445–8552. https://doi.org/10.1021/acscatal.8b01929.

(4) Hemmerling, J.; Quinn, J.; Linic, S. Quantifying Losses and Assessing the Photovoltage Limits in Metal–Insulator–Semiconductor Water Splitting Systems. *Adv. Energy Mater.* **2020**, *10* (12), 1–10. https://doi.org/10.1002/aenm.201903354.

(5) Quinn, J.; Hemmerling, J.; Linic, S. Guidelines for Optimizing the Performance of Metal-Insulator-Semiconductor (MIS) Photoelectrocatalytic Systems by Tuning the Insulator Thickness. *ACS Energy Lett.* **2019**, *4* (11), 2632–2638. https://doi.org/10.1021/acsenergylett.9b01609.

(6) Hemmerling, J. R.; Mathur, A.; Linic, S. Design Principles for Efficient and Stable Water Splitting Photoelectrocatalysts. *Acc. Chem. Res.* **2021**, *54* (8), 1992–2002. https://doi.org/10.1021/acs.accounts.1c00072.

(7) Haussener, S.; Hu, S.; Xiang, C.; Weber, A. Z.; Lewis, N. S. Simulations of the Irradiation and Temperature Dependence of the Efficiency of Tandem Photoelectrochemical Water-Splitting Systems. *Energy Environ. Sci.* **2013**, *6* (12), 3605–3618. https://doi.org/10.1039/c3ee41302k.

(8) Singh, M. R.; Haussener, S.; Weber, A. Z. Continuum-Scale Modeling of Solar Water-Splitting Devices. **2019**, No. 22, 500–536.

(9) Bae, D.; Pedersen, T.; Seger, B.; Malizia, M.; Kuznetsov, A.; Hansen, O.; Chorkendorff, I.; Vesborg, P. C. K. Back-Illuminated Si Photocathode: A Combined Experimental and Theoretical Study for Photocatalytic Hydrogen Evolution. *Energy Environ. Sci.* **2015**, *8* (2), 650–660. https://doi.org/10.1039/c4ee03723e.

(10) Park, M. J.; Jung, J. Y.; Nam, Y. H.; Song, J. W.; Jeong, C.; Lee, J. H. Improved Photoelectrochemical Hydrogen Evolution Using a Defect-Passivated Al_2O_3 Thin Film on p-Si. *Thin Solid Films* **2016**, *616*, 550–554. https://doi.org/10.1016/j.tsf.2016.09.020.

(11) Liu, J.; Hisatomi, T.; Ma, G.; Iwanaga, A.; Minegishi, T.; Moriya, Y.; Katayama, M.; Kubota, J.; Domen, K. Improving the Photoelectrochemical Activity of $La_5Ti_2CuS_5O_7$ for Hydrogen Evolution by Particle Transfer and Doping. *Energy Environ. Sci.* **2014**, *7* (7), 2239–2242. https://doi.org/10.1039/c4ee00091a.

(12) Jung, J. Y.; Kim, D. W.; Park, T. J.; Lee, J. H. Design Guidelines of Insulator for

Improving Stability and Performance of Nanoelectrocatalyst/Insulator/Semiconductor Photoelectrochemical Cells. *ACS Appl. Energy Mater.* **2020**, *3* (1), 1046–1053. https://doi.org/10.1021/acsaem.9b02070.

(13) Gaudy, Y. K.; Haussener, S. Utilizing Modeling, Experiments, and Statistics for the Analysis of Water-Splitting Photoelectrodes. *J. Mater. Chem. A* **2016**, *4* (8), 3100–3114. https://doi.org/10.1039/c5ta07328f.

(14) Haussener, S.; Xiang, C.; Spurgeon, J. M.; Ardo, S.; Lewis, N. S.; Weber, A. Z. Modeling, Simulation, and Design Criteria for Photoelectrochemical Water-Splitting Systems. *Energy Environ. Sci.* **2012**, *5* (12), 9922–9935. https://doi.org/10.1039/c2ee23187e.

(15) Creissen, C. E.; Fontecave, M. Solar-Driven Electrochemical CO_2 Reduction with Heterogeneous Catalysts. *Adv. Energy Mater.* **2020**, *11* (43), 2002652. https://doi.org/10.1002/aenm.202002652.

(16) Cheng, W. H.; Richter, M. H.; Sullivan, I.; Larson, D. M.; Xiang, C.; Brunschwig, B. S.; Atwater, H. A. CO_2 Reduction to CO with 19% Efficiency in a Solar-Driven Gas Diffusion Electrode Flow Cell under Outdoor Solar Illumination. *ACS Energy Lett.* **2020**, 470–476. https://doi.org/10.1021/acsenergylett.9b02576.

(17) Singh, M. R.; Clark, E. L.; Bell, A. T. Thermodynamic and Achievable Efficiencies for Solar-Driven Electrochemical Reduction of Carbon Dioxide to Transportation Fuels. *Proc. Natl. Acad. Sci. U. S. A.* **2015**, *112* (45), E6111–E6118. https://doi.org/10.1073/pnas.1519212112.

(18) Kalamaras, E.; Wang, H.; Mercedes Maroto-Valer, M.; Andresen, J. M.; Xuan, J. Theoretical Efficiency Limits of Photoelectrochemical CO_2 Reduction: A Route-Dependent Thermodynamic Analysis. *ChemPhysChem* **2020**, *21* (3), 232–239. https://doi.org/10.1002/cphc.201901041.

(19) Qiu, J.; Zeng, G.; Ha, M. A.; Ge, M.; Lin, Y.; Hettick, M.; Hou, B.; Alexandrova, A. N.; Javey, A.; Cronin, S. B. Artificial Photosynthesis on TiO_2-Passivated InP Nanopillars. *Nano Lett.* **2015**, *15* (9), 6177–6181. https://doi.org/10.1021/acs.nanolett.5b02511.

(20) Jang, Y. J.; Jang, J. W.; Lee, J.; Kim, J. H.; Kumagai, H.; Lee, J.; Minegishi, T.; Kubota, J.; Domen, K.; Lee, J. S. Selective CO Production by Au Coupled ZnTe/ZnO in the Photoelectrochemical CO2 Reduction System. *Energy Environ. Sci.* **2015**, *8* (12), 3597–3604. https://doi.org/10.1039/c5ee01445j.

(21) Gurudayal; Beeman, J. W.; Bullock, J.; Wang, H.; Eichhorn, J.; Towle, C.; Javey, A.; Toma, F. M.; Mathews, N.; Ager, J. W. Si Photocathode with Ag-Supported Dendritic Cu Catalyst for CO2 Reduction. *Energy Environ. Sci.* **2019**, *12* (3), 1068–1077. https://doi.org/10.1039/c8ee03547d.

(22) Wen, P.; Li, H.; Ma, X.; Lei, R.; Wang, X.; Geyer, S. M.; Qiu, Y. A Colloidal ZnTe Quantum Dot-Based Photocathode with a Metal-Insulator-Semiconductor Structure towards Solar-Driven CO_2 reduction to Tunable Syngas. *J. Mater. Chem. A* **2021**, *9* (6), 3589–3596. https://doi.org/10.1039/d0ta10394b.

(23) Wang, K.; Ma, Y.; Liu, Y.; Qiu, W.; Wang, Q.; Yang, X.; Liu, M.; Qiu, X.; Li, W.; Li, J.

Insights into the Development of Cu-Based Photocathodes for Carbon Dioxide (CO_2) Conversion. *Green Chem.* **2021**, *23* (9), 3207–3240. https://doi.org/10.1039/d0gc04417b.

(24) Nitopi, S.; Bertheussen, E.; Scott, S. B.; Liu, X.; Engstfeld, A. K.; Horch, S.; Seger, B.; Stephens, I. E. L.; Chan, K.; Hahn, C.; Nørskov, J. K.; Jaramillo, T. F.; Chorkendorff, I. Progress and Perspectives of Electrochemical CO_2 Reduction on Copper in Aqueous Electrolyte. *Chem. Rev.* **2019**, *119* (12), 7610–7672. https://doi.org/10.1021/acs.chemrev.8b00705.

(25) Kuhl, K. P.; Cave, E. R.; Abram, D. N.; Jaramillo, T. F. New Insights into the Electrochemical Reduction of Carbon Dioxide on Metallic Copper Surfaces. *Energy Environ. Sci.* **2012**, *5* (5), 7050–7059. https://doi.org/10.1039/c2ee21234j.

(26) De Souza, M. K. R.; Cardoso, E. D. S. F.; Fortunato, G. V.; Lanza, M. R. V.; Nazário, C. E.; Zanoni, M. V. B.; Maia, G.; Cardoso, J. C. Combination of Cu-Pt-Pd Nanoparticles Supported on Graphene Nanoribbons Decorating the Surface of TiO_2 nanotube Applied for CO_2 photoelectrochemical Reduction. *J. Environ. Chem. Eng.* **2021**, *9* (4), 105803. https://doi.org/10.1016/j.jece.2021.105803.

(27) Hinogami, R.; Nakamura, Y.; Yae, S.; Nakato, Y. An Approach to Ideal Semiconductor Electrodes for Efficient Photoelectrochemical Reduction of Carbon Dioxide by Modification with Small Metal Particles. *J. Phys. Chem. B* **1998**, *102* (6), 974–980. https://doi.org/10.1021/jp972663h.

(28) Fountaine, K. T.; Lewerenz, H. J.; Atwater, H. A. Efficiency Limits for Photoelectrochemical Water-Splitting. *Nat. Commun.* **2016**, *7*, 1–9. https://doi.org/10.1038/ncomms13706.

(29) Bui, J. C.; Kim, C.; Weber, A. Z.; Bell, A. T. Dynamic Boundary Layer Simulation of Pulsed CO_2 Electrolysis on a Copper Catalyst. *ACS Energy Lett.* **2021**, *6* (4), 1181–1188. https://doi.org/10.1021/acsenergylett.1c00364.

(30) Singh, M. R.; Clark, E. L.; Bell, A. T. Effects of Electrolyte, Catalyst, and Membrane Composition and Operating Conditions on the Performance of Solar-Driven Electrochemical Reduction of Carbon Dioxide. *Phys. Chem. Chem. Phys.* **2015**, *17* (29), 18924–18936. https://doi.org/10.1039/c5cp03283k.

(31) Gutierrez, R. R.; Haussener, S. Modeling of Concurrent CO_2 and Water Splitting by Practical Photoelectrochemical Devices . *J. Electrochem. Soc.* **2016**, *163* (10), H1008–H1018. https://doi.org/10.1149/2.0661610jes.

(32) Chen, Y.; Lewis, N. S.; Xiang, C. Modeling and Simulation of the Spatial and Light-Intensity Dependence of Product Distributions in an Integrated Photoelectrochemical CO_2 Reduction System. *ACS Energy Lett.* **2016**, *1* (1), 273–280. https://doi.org/10.1021/acsenergylett.6b00134.

(33) Hammerschmidt, M.; Döpking, S.; Burger, S.; Matera, S. Field Heterogeneities and Their Impact on Photocatalysis: Combining Optical and Kinetic Monte Carlo Simulations on the Nanoscale. *J. Phys. Chem. C* **2020**, *124* (5), 3177–3187. https://doi.org/10.1021/acs.jpcc.9b11469.

(34) Wang, Y.; Tian, Y.; Yan, L.; Su, Z. DFT Study on Sulfur-Doped g-C_3N_4 Nanosheets as a Photocatalyst for CO_2 Reduction Reaction. *J. Phys. Chem. C* **2018**, *122* (14), 7712–7719. https://doi.org/10.1021/acs.jpcc.8b00098.

(35) Ješić, D.; Lašič Jurković, D.; Pohar, A.; Suhadolnik, L.; Likozar, B. Engineering Photocatalytic and Photoelectrocatalytic CO_2 Reduction Reactions: Mechanisms, Intrinsic Kinetics, Mass Transfer Resistances, Reactors and Multi-Scale Modelling Simulations. *Chem. Eng. J.* **2021**, *407* (August 2020), 126799. https://doi.org/10.1016/j.cej.2020.126799.

(36) Pipornpong, W.; Wanbayor, R.; Ruangpornvisuti, V. Adsorption CO_2 on the Perfect and Oxygen Vacancy Defect Surfaces of Anatase TiO_2 and Its Photocatalytic Mechanism of Conversion to CO. *Appl. Surf. Sci.* **2011**, *257* (24), 10322–10328. https://doi.org/10.1016/j.apsusc.2011.06.013.

(37) Resasco, J.; Chen, L. D.; Clark, E.; Tsai, C.; Hahn, C.; Jaramillo, T. F.; Chan, K.; Bell, A. T. Promoter Effects of Alkali Metal Cations on the Electrochemical Reduction of Carbon Dioxide. *J. Am. Chem. Soc.* **2017**, *139* (32), 11277–11287. https://doi.org/10.1021/jacs.7b06765.

(38) Ringe, S.; Clark, E. L.; Resasco, J.; Walton, A.; Seger, B.; Bell, A. T.; Chan, K. Understanding Cation Effects in Electrochemical CO_2 Reduction. *Energy Environ. Sci.* **2019**, *12* (10), 3001–3014. https://doi.org/10.1039/c9ee01341e.

(39) Bui, J. C.; Kim, C.; King, A. J.; Romiluyi, O.; Kusoglu, A.; Weber, A. Z.; Bell, A. T. Engineering Catalyst − Electrolyte Microenvironments to Optimize the Activity and Selectivity for the Electrochemical Reduction of CO_2 on Cu and Ag. *Acc. Chem. Res.* **2021**, *55* (4), 484–494. https://doi.org/10.1021/acs.accounts.1c00650.

(40) Singh, M. R.; Kwon, Y.; Lum, Y.; Ager, J. W.; Bell, A. T. Hydrolysis of Electrolyte Cations Enhances the Electrochemical Reduction of CO_2 over Ag and Cu. *J. Am. Chem. Soc.* **2016**, *138* (39), 13006–13012. https://doi.org/10.1021/jacs.6b07612.

(41) Resasco, J.; Lum, Y.; Clark, E.; Zeledon, J. Z.; Bell, A. T. Effects of Anion Identity and Concentration on Electrochemical Reduction of CO_2. *ChemElectroChem* **2018**, *5* (7), 1064–1072. https://doi.org/10.1002/celc.201701316.

(42) Maier, C. U.; Specht, M.; Bilger, G. Hydrogen Evolution on Platinum-Coated p-Silicon Photocathodes. *Int. J. Hydrogen Energy* **1996**, *21* (10), 859–864. https://doi.org/10.1016/0360-3199(96)00023-7.

(43) Laskowski, F. A. L.; Oener, S. Z.; Nellist, M. R.; Gordon, A. M.; Bain, D. C.; Fehrs, J. L.; Boettcher, S. W. Nanoscale Semiconductor/Catalyst Interfaces in Photoelectrochemistry. *Nat. Mater.* **2020**, *19* (1), 69–76. https://doi.org/10.1038/s41563-019-0488-z.

(44) Kim, C.; Bui, J. C.; Luo, X.; Cooper, J. K.; Kusoglu, A.; Weber, A. Z.; Bell, A. T. Tailored Catalyst Microenvironments for CO_2 Electroreduction to Multicarbon Products on Copper Using Bilayer Ionomer Coatings. *Nat. Energy* **2021**, *6* (11), 1026–1034. https://doi.org/10.1038/s41560-021-00920-8.

(45) Sze, S. M.; Ng, K. K. *Physics of Semiconductor Devices*; John Wiley: New York, 1981.

(46) Polman, A.; Knight, M.; Garnett, E. C.; Ehrler, B.; Sinke, W. C. Photovoltaic Materials: Present Efficiencies and Future Challenges. *Science (80-.).* **2016**, *352* (6283). https://doi.org/10.1126/science.aad4424.

(47) Kim, C.; Weng, L. C.; Bell, A. T. Impact of Pulsed Electrochemical Reduction of CO_2 on the Formation of C_{2+} Products over Cu. *ACS Catal.* **2020**, *10* (21), 12403–12413. https://doi.org/10.1021/acscatal.0c02915.

(48) Sengupta, M.; Xie, Y.; Lopez, A.; Habte, A.; Maclaurin, G.; Shelby, J. The National Solar Radiation Data Base (NSRDB). *Renew. Sustain. Energy Rev.* **2018**, *89* (January 2018), 51–60. https://doi.org/10.1016/j.rser.2018.03.003.

(49) Haussener, S.; Hu, S.; Xiang, C.; Weber, A. Z.; Lewis, N. S. Simulations of the Irradiation and Temperature Dependence of the Efficiency of Tandem Photoelectrochemical Water-Splitting Systems. *ECS Transactions*. 2013, pp 293–303. https://doi.org/10.1149/05802.0293ecst.

For Table of Contents Only